LETTER

doi:10.1038/nature12877

Worldwide acceleration of mountain erosion under a cooling climate

Frédéric Herman[1,2], Diane Seward[3], Pierre G. Valla[1,2], Andrew Carter[4], Barry Kohn[5], Sean D. Willett[2] & Todd A. Ehlers[6]

Climate influences the erosion processes acting at the Earth's surface. However, the effect of cooling during the Late Cenozoic era, including the onset of Pliocene–Pleistocene Northern Hemisphere glaciation (about two to three million years ago), on global erosion rates remains unclear[1–4]. The uncertainty arises mainly from a lack of consensus on the use of the sedimentary record as a proxy for erosion[3,4] and the difficulty of isolating the respective contributions of tectonics and climate to erosion[5–7]. Here we compile 18,000 bedrock thermochronometric ages from around the world and use a formal inversion procedure[8] to estimate temporal and spatial variations in erosion rates. This allows for the quantification of erosion for the source areas that ultimately produce the sediment record on a timescale of millions of years. We find that mountain erosion rates have increased since about six million years ago and most rapidly since two million years ago. The increase of erosion rates is observed at all latitudes, but is most pronounced in glaciated mountain ranges, indicating that glacial processes played an important part. Because mountains represent a considerable fraction of the global production of sediments[9], our results imply an increase in sediment flux at a global scale that coincides closely with enhanced cooling during the Pliocene and Pleistocene epochs[10,11].

The Earth's continental topography reflects the balance between tectonics and climate, and their interaction through erosion. Therefore, any change in either climate or tectonics is expected to lead to a change in topography and erosion rates. In that context, Late Cenozoic global cooling represents one of the best-documented major shifts in climate. During this transition, the climate cooled and evolved towards high-amplitude oscillating conditions that are associated with the waxing and waning of continental ice sheets in the Northern Hemisphere and alpine glaciers throughout the Pliocene and Pleistocene epochs[10,11]. As a consequence of these oscillations, the climate's influence on erosion became highly variable. In particular, it continuously switched between fluvial and (peri)glacial processes in many mid- to high-latitude, high-elevation regions[1,2]. Several studies have documented locally an increase of erosion in response to this climate transition[12–18], although the timing and magnitude of this erosional shift vary with latitude. However, whether this effect can explain the apparent global increase in sediment accumulation remains a subject of debate. The controversy comes from an observed increase in sediment accumulation rates, which may be biased by the incompleteness of the sedimentary record[3,4].

To address this issue, we quantify erosion rates at an unprecedented global scale directly from bedrock using low-temperature thermochronometry. Thermochronometry exploits the diffusion behaviour of noble gases through crystals, or damage trails produced by the spontaneous fission of ^{238}U contained in target minerals, to interpret measured apparent ages in terms of the travel time of a rock from a given closure temperature (at which diffusion/annealing becomes negligible) to the surface (see ref. 19 for a review). The passage of a rock through a temperature field near the Earth's surface gives its thermochronometric age, which can be converted into a cooling history and subsequently into an erosion rate integrated over the timescale provided by the measured age. We compiled data from across the globe for four low-temperature thermochronometric systems: apatite (U–Th)/He, apatite fission track, zircon (U–Th)/He and zircon fission track, which have approximate closure temperatures of 70 °C, 110 °C, 180 °C and 250 °C, respectively[19]. Taken together, these thermochronometers enable the tracking of bedrock erosion from typical crustal depths of about 8–10 km (ref. 19) up to the surface. Furthermore, by using multiple thermochronometers, and taking note of the information contained in the elevation at which bedrock samples were acquired, we are able to resolve recent variability in erosion rates. In total, 17,833 thermochronometric ages were compiled worldwide (Extended Data Fig. 1). Unlike sediment accumulation budgets[3,4], which are subject to many assumptions about transport and deposition, thermochronometry provides a first-order unbiased estimate of erosion in the bedrock source regions.

To estimate the rates of erosion in space and time, we perform a formal analysis of the compiled thermochronometric data using a new approach[8] based on linear inverse theory (Methods). This procedure enables the efficient treatment of a large number of spatially distributed data and provides an explicit definition of variance and resolution, which can be used to determine where erosion rates are well resolved both in space and time. We focus on the results from the past 8 million years (Myr), for which resolution is high enough to resolve potential changes in erosion rates (that is, where we might see variations associated with the onset of Pliocene–Pleistocene Northern Hemisphere glaciation). A limitation to our approach is that we do not consider complexities in the data related to small-scale tectonic structures. We expect such regional effects to be negligible at a global scale (Methods). Similarly, we do not consider uncertainties on the kinetic parameters of each thermochronometric system.

Results indicate that erosion rates vary globally since 8 Myr ago within four orders of magnitude, ranging from less than 0.01 mm yr^{-1} up to about 10 mm yr^{-1} (Fig. 1 and Supplementary Video). The slowest-eroding regions (<0.01 mm yr^{-1}) for which we have thermochronometric data are cratonic areas of central and western Australia, central North America and eastern Scandinavia. Rates are higher (0.01–0.1 mm yr^{-1}) in the passive margins of southeastern Australia, Brazil, the eastern USA, western Scandinavia, Madagascar, South Africa, Sri Lanka, southern India, the Tibetan plateau and its margins, and the Altiplano. Most of these thermochronometric age-derived erosion rates are integrated over several tens to hundreds of million years and, therefore, have insufficient resolution to reveal temporal variations associated with the Late Cenozoic cooling and Pliocene–Pleistocene glaciation. As an illustration, the authors of ref. 18 recently used the Pliocene–Pleistocene offshore sediment record and a palaeo-topographic reconstruction to identify an increase in erosion by a factor of 20 (from ~0.01 mm yr^{-1} up to ~0.2 mm yr^{-1}) during the Pliocene–Pleistocene in western Scandinavia, which they attributed to a switch from fluvial to glacial erosion. Even with this

[1]Institute of Earth Sciences, University of Lausanne, CH-1015 Lausanne, Switzerland. [2]Department of Earth Sciences, Swiss Federal Institute of Technology, Sonneggstrasse 6, CH-8092 Zürich, Switzerland. [3]School of Geography, Environment and Earth Sciences, Victoria University, PO Box 600, Wellington, New Zealand. [4]Department of Earth and Planetary Science, Birkbeck University of London, Malet Street, Bloomsbury, London WC1E 7HX, UK. [5]School of Earth Sciences, University of Melbourne, Victoria 3010, Australia. [6]Department of Geosciences, University of Tübingen, Wilhelmstrasse 56, D-72074 Tübingen, Germany.

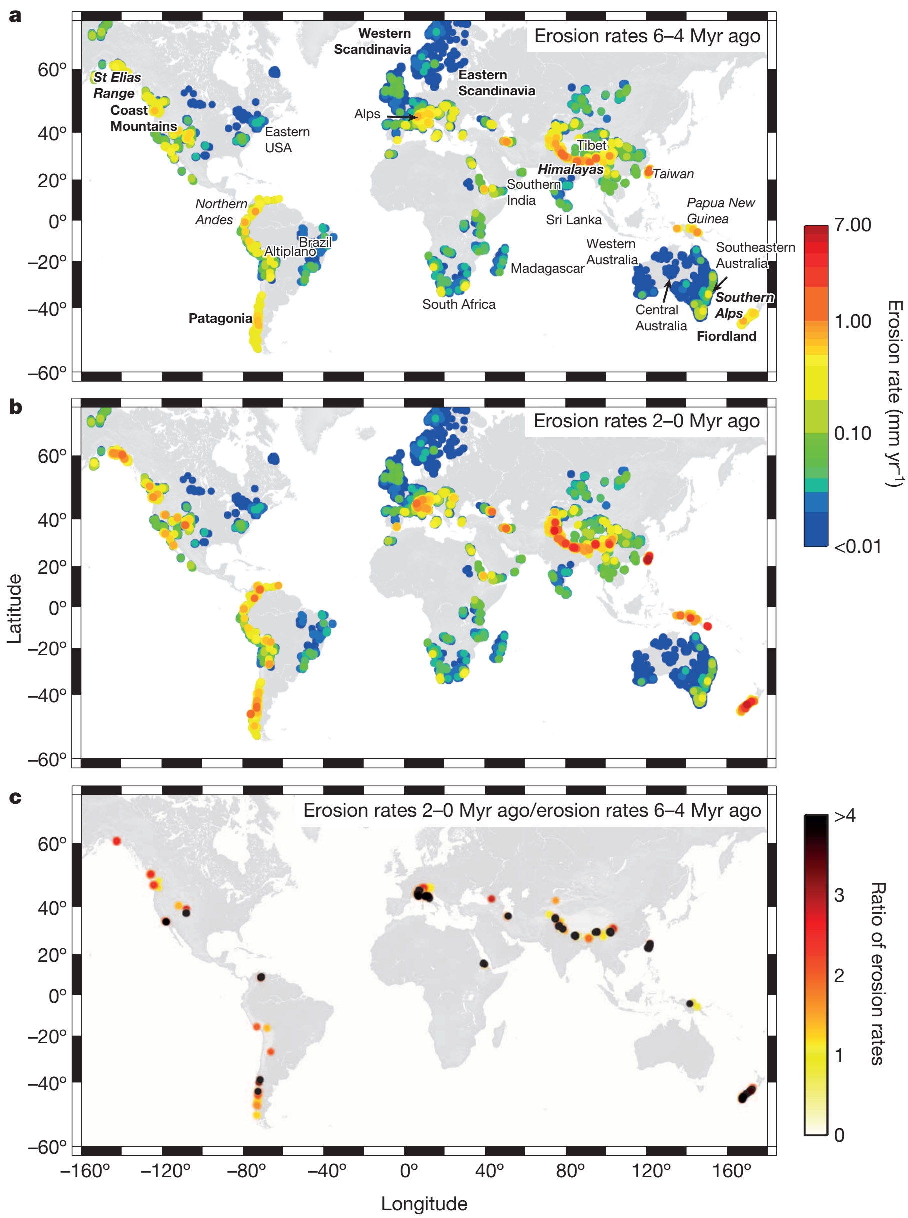

Figure 1 | Erosion rates and their variations over the past 6 Myr, resolved into 2-Myr time steps. **a**, Erosion rates between 6 Myr ago and 4 Myr ago. **b**, Erosion rates between 2 Myr ago and 0 Myr ago. **c**, Ratio of erosion rates between 2–0 Myr ago and 6–4 Myr ago, where resolution is higher than 0.25. We use a time step length of 2 Myr for ages younger than 40 Myr ago, and a 40-Myr time step for ages older than 40 Myr ago. The initial geotherm is equal to 26 °C km^{-1}. We use a thermal diffusivity equal to 30 km^2 Myr^{-1} and a 50-km vertical extent. The a priori erosion rates are set to 0.35 ± 0.1 mm yr^{-1} in tectonically active mountain ranges and 0.01 ± 0.01 mm yr^{-1} in tectonically inactive regions. Italic font indicates tectonically active mountain ranges and boldface font indicates glaciated ranges mentioned in the text.

significant increase in rate, the total erosion remains too small to be detected by any of the thermochronometric systems we have considered (Fig. 1).

Erosion rates are significantly higher (2–7 mm yr^{-1}) in several tectonically active mountainous areas (Fig. 1) (for example, the Southern Alps of New Zealand, Taiwan, Papua New Guinea, the Himalayas and the St Elias Range of Alaska). These orogens also receive significant precipitation[7], which can sustain high erosion rates. These areas are either glaciated or exhibit threshold hillslopes, dominated by landslides, which are a characteristic of high erosion rates[20]. Also, we observe rates higher than 1 mm yr^{-1} in some tectonically quiescent orogens such as the western European Alps, the Coast Mountains of British Columbia, Fiordland in New Zealand or northern Patagonia. In contrast with some of the more tectonically active areas, we observe high rates only in quiescent areas where the topography was heavily affected by glacial erosion[12–18].

Our results highlight an increase in erosion during the Late Cenozoic in most mountain ranges (Figs 1b and c, 2 and 3). The majority of the increase in erosion rates we detect is based on the difference in cooling from apatite fission track to apatite (U–Th)/He closure depth. Our results therefore depend partly on the thermal model and kinetic parameters we prescribe for each system in the inversion scheme. We first evaluate the significance of this erosion rate increase by computing the ratio of erosion rates 2–0 Myr ago to those 6–4 Myr ago, limiting our analysis to regions where the thermochronological cooling history is well resolved (that is, resolution is higher than 0.25, which is chosen arbitrarily; see Methods). The distribution of erosion rates shows that more than 80% of the regions with high-resolution values exhibit an increase, with an erosion rate ratio between >1 and 4 (Fig. 2). This increase is observed at all latitudes, but is more pronounced at latitudes outside the intertropical zone (inset of Fig. 2). The increase of erosion rate in low-latitude, non-glaciated regions (that is, <25°) may locally correspond to recent tectonic activity (for example, Papua New Guinea, Taiwan, the Red Sea or the northern Andes) but may also be associated with enhanced climatic variability[1,2]. Interestingly, we do not observe an increase of erosion rate in tectonically inactive regions at low latitudes. It may be that either the increase is not sufficiently large to be resolved by the thermochronometric data we compiled or there is a bias related to the spatial distribution of ages and the location of mountain ranges on Earth (such as that there are fewer mountain ranges at latitudes below 25°). At intermediate latitudes of 25°–50°, substantial changes in erosion rates are observed. In the Himalayas, rates have been consistently high over the past 8 Myr, but have increased in the northern high-elevation glaciated regions of the Greater Himalaya Sequence during the past 4 Myr,

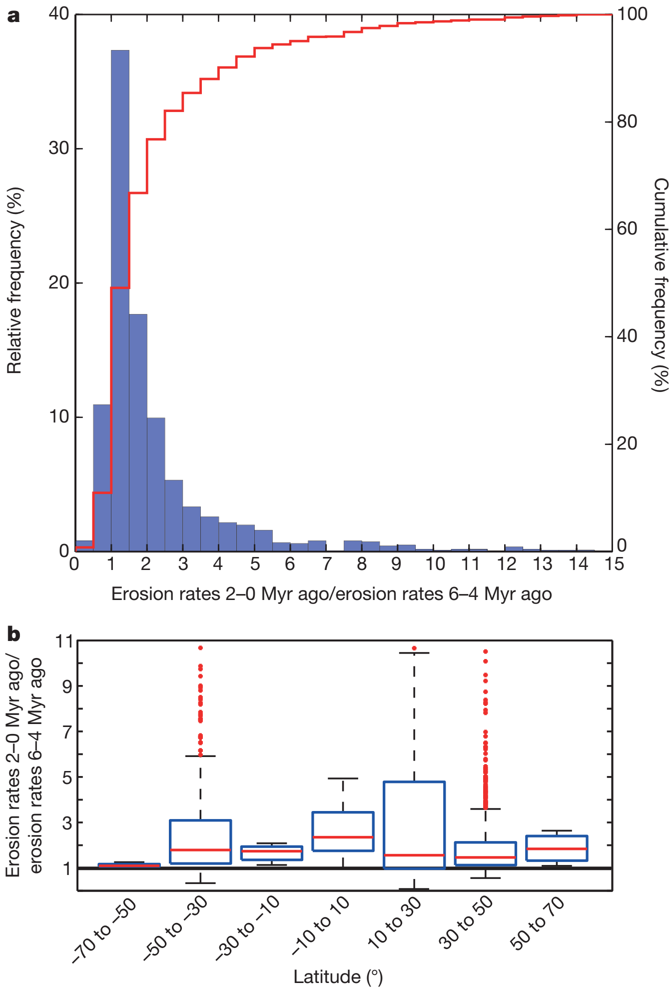

Figure 2 | **Relative frequency and cumulative distributions of the ratio of erosion rates between 2–0 Myr ago and 6–4 Myr ago.** **a**, Blue bars depict the relative frequency and the red line the cumulative distribution. The reported values are computed only at locations where the erosion rate is estimated and the resolution is higher than 0.25. Values higher than 1 indicate an increase of erosion rates and lower than 1 indicate a decrease. **b**, A box-and-whisker plot of the data used in this calculation distributed over latitude (using 20° intervals). The red line in each box is the median, the edges of the box are the 25th and 75th percentiles, the whiskers extend to the most extreme data points not considered outliers, and outliers are plotted as red dots.

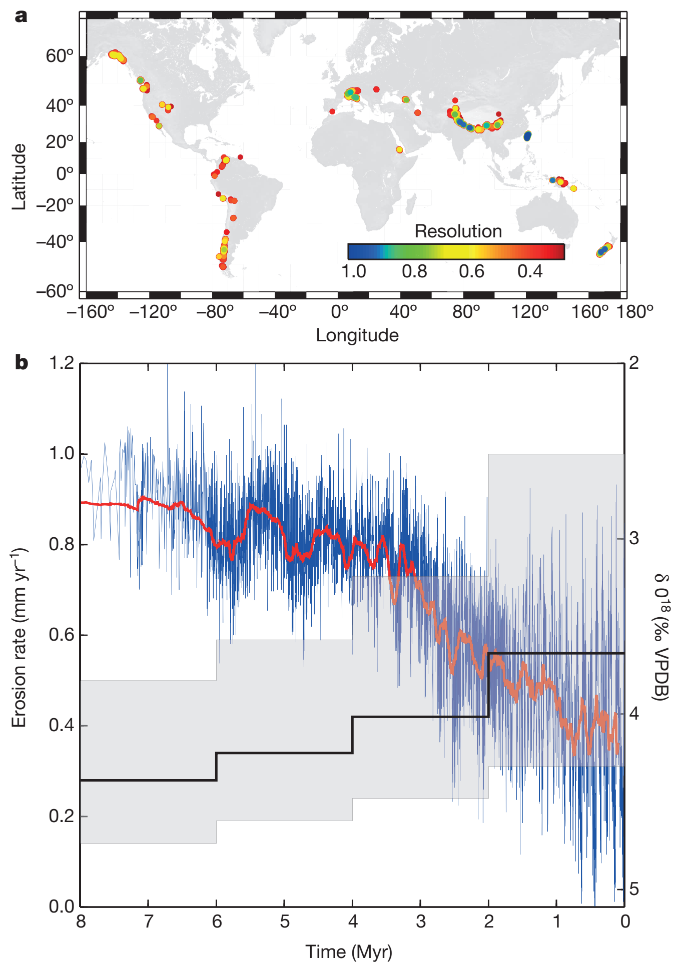

Figure 3 | **Mountain erosion rates and δ^{18}O measurements during the Late Cenozoic era.** **a**, Resolution is higher than 0.25 for the past 2 Myr. **b**, Erosion rate is computed at locations shown in **a**. The median (black line) and standard deviation (grey area) are estimated from the distributions of erosion rates over each 2-Myr time interval. (There is no weighting correction for areal coverage, except from using the solution at the grid points; see Methods.) The blue line depicts the raw δ^{18}O data compilation[11], whereas the red line corresponds to the moving average. VPDB, the Vienna Pee-Dee belemnite standard.

in spite of steady convergence rates[21]. In the past 2 Myr, very large changes in erosion rates are observed at latitudes above 30° (for example, the European Alps, Patagonia, Alaska, the South Island of New Zealand and the Coast Mountains of British Columbia). These areas are highly variable in their tectonic activity, but they have all been glaciated in the past few million years. This further suggests that glacial erosion has played an important part globally.

Collapsing erosion rates in mountainous areas to a median and variance over each 2-Myr time interval (Fig. 3) reveals an increase in mountain erosion rates since about 6 Myr ago, by nearly a factor of two for the Pleistocene compared to the Pliocene. This change shows a clear temporal correspondence with further cooling and increased amplitude of glacial cycles, as indicated by the global compilation of benthic foraminifera δ^{18}O measurements[11], which serve as a proxy for reconstructing global climate fluctuations. Such a short-term shift in erosion rates must be climate-driven, given that a global acceleration in tectonic activity is unlikely[1,2].

The global increase in erosion has been attributed primarily to enhanced climate variability during the Late Cenozoic era and the Pliocene–Pleistocene epoch[1,2]. Such variability may play a part in low-latitude regions where fluvial erosion dominates. Recent modelling and observational studies suggest that erosion can be promoted by an increase in both mean runoff and discharge variability[22,23]. However, our inversion of thermochronometric data does not have enough resolving power to reveal large changes in erosion rates in areas that are both fluvial-dominated and tectonically inactive. In terms of the effects of glaciers and ice caps on erosion rates, strong nonlinear feedbacks exist between glacial erosion, landscape hypsometry, net mass ice balance, climate and tectonics, all of which make attributing an increase of erosion mainly to climatic oscillations less obviously justifiable. In fact, modelling efforts have shown that glacial erosion predominantly increases in response to increased ice accumulation area owing to enhanced climate cooling[24,25], surface uplift or both[25]. Although repeated alteration between fluvial and glacial processes may have played a part[1,2], the pronounced cooling during the Pliocene–Pleistocene would be sufficient to induce an increase of erosion rates in glaciated mountain regions.

Our observations establish that the rates at which mountainous landscapes have eroded increased globally during the Late Cenozoic and that this increase correlates with further cooling and an increase of the amplitude of climate cycles. This effect is observed not only in tectonically active mountain ranges, but also in relatively inactive orogens that have experienced glacial erosion (for example, the western Alps, the Coast Mountains of British Columbia, Patagonia). This increase has global implications under the assumption that mountains dominate global sediment production[9]. Recently, the authors of ref. 26 suggested that mountains have less of a role in erosion than do flat terrains. However, they derived and used a biased relationship between slope and denudation that led to an underestimation of sediment production from steep terrains (J. K. Willenbring, personal communication, 2013).

Furthermore, our inferred increase in the Late Cenozoic erosion rates supports an erosional feedback on climate, that is, the carbon dioxide (CO_2) cycle and its connections to Pliocene–Pleistocene cooling. Late Cenozoic cooling has been related to decreasing atmospheric CO_2, including a sharp drop in CO_2 at about 3 Myr ago (refs 27 and 28). Two main mechanisms linked to increased erosion could contribute to this CO_2 drawdown. First, an increase in physical erosion could lead to increased silicate weathering, which serves as a CO_2 sink (see ref. 29, for example), although some authors have recently argued that weathering is not necessarily associated with physical erosion[30,31]. Second, burial of terrestrial organic carbon[31] can be very efficient at sequestering CO_2 in the ocean. This process is clearly correlated with physical erosion rate[32] and may explain the tight temporal connection we observe between a change in climate and erosion. Either or both of these mechanisms could result in a strong positive feedback between climate and erosion, in which carbon dioxide removal from the atmosphere is enhanced by erosion, thereby promoting cooling.

METHODS SUMMARY

Inversion of thermochronological data. We use the method developed by ref. 8 to invert thermochronometric data sets. It exploits the information contained in both age–elevation profiles and multi-thermochronometric systems strategies. In this approach, the depth to the closure temperature is an integral of erosion rate from the thermochronometric age to the present day. This closure depth is computed using a one-dimensional thermal model combined with a spectral solution that accounts for the effects of topography on the isotherms. Erosion rate is parameterized as a piecewise constant function over fixed time intervals. A thermochronometric age is thus represented by a linear equation, and a suite of n thermochronometric ages becomes a linear system of equations:

$$A\dot{e} = z_c \tag{1}$$

where z_c is a vector of length n describing the different closure depths, $\dot{e}$ is a vector of unknown erosion rates and A is a sparse matrix whose components have units of time. To solve these independent equations, we impose a condition that erosion rates are correlated in space by defining an a priori covariance matrix, C. This matrix is constructed using the separation distance d between the ith and jth data points and an exponential correlation function:

$$C_{ij} = \sigma_e^2 e^{-\frac{d}{\lambda}} \tag{2}$$

where λ is a specified correlation length that we fix equal to 30 km. The a priori variance for the erosion rate, σ_e^2, serves primarily as a weighting factor. In turn, the maximum likelihood estimate for the erosion rate, $\dot{e}$, is given by:

$$\dot{e} = \dot{e}_{pr} + CA^T(ACA^T + C_\varepsilon)^{-1}(z_c - A\dot{e}_{pr}) \tag{3}$$

where $\dot{e}_{pr}$ is the a priori expected value of the erosion rate and C_ε is a diagonal matrix containing the estimated data uncertainty. We calculated a parameter resolution matrix, R, as:

$$R = CA^T\,(ACA^T + C_\varepsilon)^{-1}A \tag{4}$$

which permits us to establish when changes in erosion rates are well resolved. This is integrated across the spatial dimension. Results at data locations are then interpolated on a regular grid for visualization and to reduce weight due to the sampling density.

Online Content Any additional Methods, Extended Data display items and Source Data are available in the online version of the paper; references unique to these sections appear only in the online paper.

Received 16 June; accepted 13 November 2013.

1. Zhang, P., Molnar, P. & Downs, W. R. Increased sedimentation rates and grain sizes 2–4 Myr ago due to the influence of climate change on erosion rates. *Nature* **410,** 891–897 (2001).
2. Molnar, P. Late Cenozoic increase in accumulation rates of terrestrial sediment: how might climate change have affected erosion rates? *Annu. Rev. Earth Planet. Sci.* **32,** 67–89 (2004).
3. Schumer, R. & Jerolmack, D. J. Real and apparent changes in sediment deposition rates through time. *J. Geophys. Res.* **114,** F00A06 (2009).
4. Willenbring, J. K. & von Blanckenburg, F. Long-term stability of global erosion rates and weathering during late-Cenozoic cooling. *Nature* **465,** 211–214 (2010).
5. von Blanckenburg, F. The control mechanism of erosion and weathering at basin scale from cosmogenic nuclides in river sediments. *Earth Planet. Sci. Lett.* **237,** 462–479 (2005).
6. Whipple, K. X. The influence of climate on the tectonic evolution of mountain belts. *Nature Geosci.* **2,** 97–104 (2009).
7. Champagnac, J.-D., Molnar, P., Sue, C. & Herman, F. Tectonics, climate, and mountain topography. *J. Geophys. Res.* **117,** B02403 (2012).
8. Fox, M., Herman, F., Willett, S. D. & May, A. D. A linear inversion method to infer exhumation rates in space and time from thermochronometric data. *Earth Surf. Dynam. Discuss.* **1,** 207–259 (2013).
9. Milliman, J. D. & Syvitski, J. P. M. Geomorphic/tectonic control of sediment discharge to the ocean: the importance of small mountainous rivers. *J. Geol.* **100,** 525–544 (1992).
10. Shackleton, N. J. & Opdyke, N. D. Oxygen isotope and paleomagnetic evidence for early Northern Hemisphere glaciation. *Nature* **270,** 216–219 (1977).
11. Zachos, J., Pagani, M., Sloan, L., Thomas, E. & Billups, K. Trends, rhythms, and aberrations in global climate 65 Ma to present. *Science* **292,** 686–693 (2001).
12. Shuster, D. L., Ehlers, T. A., Rusmore, M. E. & Farley, K. A. Rapid glacial erosion at 1.8 Ma revealed by $^4He/^3He$ thermochronometry. *Science* **310,** 1668–1670 (2005).
13. Berger, A. L. *et al.* Quaternary tectonic response to intensified glacial erosion in an orogenic wedge. *Nature Geosci.* **1,** 793–799 (2008).
14. Vernon, A. J., van der Beek, P. A., Sinclair, H. D. & Rahn, M. K. Increase in late Neogene denudation of the European Alps confirmed by analysis of a fission track thermochronology database. *Earth Planet. Sci. Lett.* **270,** 316–329 (2008).
15. Thomson, S. N. *et al.* Glaciation as a destructive and constructive control on mountain building. *Nature* **467,** 313–317 (2010).
16. Shuster, D. L., Cuffey, K. M., Sanders, J. W. & Balco, G. Thermochronometry reveals headward propagation of erosion in an alpine landscape. *Science* **332,** 84–88 (2011).
17. Valla, P. G. *et al.* Late Neogene exhumation and relief development of the Aar and Aiguilles Rouges massifs (Swiss Alps) from low-temperature thermochronology modeling and $^4He/^3He$ thermochronometry. *J. Geophys. Res.* **117,** F01004 (2012).
18. Steer, P., Huismans, R. S., Valla, P. G., Gac, S. & Herman, F. Bimodal Plio-Quaternary glacial erosion of fjords and low-relief surfaces in Scandinavia. *Nature Geosci.* **5,** 635–639 (2012).
19. Reiners, P. W. & Brandon, M. T. Using thermochronology to understand orogenic erosion. *Annu. Rev. Earth Planet Sci.* **34,** 419–466 (2006).
20. Montgomery, D. R. & Brandon, M. T. Topographic controls on erosion rates in tectonically active mountain ranges. *Earth Planet. Sci. Lett.* **201,** 481–489 (2002).
21. Thiede, R. C. & Ehlers, T. A. Large spatial and temporal variations in Himalayan denudation. *Earth Planet. Sci. Lett.* **371–372,** 278–293 (2013).
22. Lague, D., Hovius, N. & Davy, P. Discharge, discharge variability, and the bedrock channel profile. *J. Geophys. Res.* **110,** F04006 (2005).
23. DiBiase, R. A. & Whipple, K. X. The influence of erosion thresholds and runoff variability on the relationships among topography, climate, and erosion rate. *J. Geophys. Res.* **116,** F04036 (2011).
24. Pedersen, V. K. & Egholm, D. L. Glaciations in response to climate variations preconditioned by evolving topography. *Nature* **493,** 206–210 (2013).
25. Sternai, P., Herman, F., Valla, P. G. & Champagnac, J.-D. Spatial and temporal variations of glacial erosion in the Rhone valley (Swiss Alps): insights from numerical modeling. *Earth Planet. Sci. Lett.* **368,** 119–131 (2013).
26. Willenbring, J. K., Codilean, A. T. & McElroy, B. Earth is (mostly) flat: apportionment of the flux of continental sediment over millennial time scales. *Geology* **41,** 343–346 (2013).
27. Seki, O. *et al.* Alkenone and boron-based Pliocene pCO_2 records. *Earth Planet. Sci. Lett.* **292,** 201–211 (2010).
28. Bartoli, G., Hönisch, B. & Zeebe, R. E. Atmospheric CO_2 decline during the Pliocene intensification of Northern Hemisphere glaciations. *Paleoceanography* **26,** PA4213 (2011).
29. Raymo, M. E., Ruddiman, W. F. & Froelich, P. N. Influence of late Cenozoic mountain building on ocean geochemical cycles. *Geology* **16,** 649–653 (1988).
30. Moore, J., Jacobson, A. D., Holmden, C. & Craw, D. Tracking the relationship between mountain uplift, silicate weathering, and long-term CO_2 consumption with Ca isotopes: southern Alps, New Zealand. *Chem. Geol.* **341,** 110–127 (2013).
31. West, A. J., Galy, A. & Bickle, M. Tectonic and climatic controls on silicate weathering. *Earth Planet. Sci. Lett.* **235,** 211–228 (2005).
32. Galy, V. *et al.* Efficient organic carbon burial in the Bengal fan sustained by the Himalayan erosional system. *Nature* **450,** 407–410 (2007).

Supplementary Information is available in the online version of the paper.

Acknowledgements We thank J.-D. Champagnac and M. Brandon for discussions throughout the study. We also thank S. Jaccard and P. Molnar for their feedback on the manuscript and K. Huntington for her constructive review. The computations presented here were performed on the Brutus facility at ETH Zurich, Switzerland. F.H. was funded by SNF grant PP00P2_138956.

Author Contributions F.H. designed the study and carried out the data interpretation. F.H., D.S., P.G.V., A.C., B.K. and T.A.E. contributed to compiling the data. All authors contributed to writing the paper.

Author Information Reprints and permissions information is available at www.nature.com/reprints. The authors declare no competing financial interests. Readers are welcome to comment on the online version of the paper. Correspondence and requests for materials should be addressed to F.H. (frederic.herman@unil.ch).

METHODS

Inversion of thermochronological data. We use the method recently developed by ref. 8 to invert thermochronometric data sets. It exploits the information contained in both age–elevation profiles and multi-thermochronometric systems strategies. In this approach, we express the depth to the closure temperature as the integral of erosion rate from the thermochronometric age to present-day as:

$$\int_0^{\tau} \dot{e}(t)\mathrm{d}t = z_c \quad (1)$$

where z_c is the closure depth, τ is the thermochronometric age and $\dot{e}$ the erosion rate. We wish to solve for $\dot{e}$, which can be achieved given that the depth of closure is estimated. To that end, we use a one-dimensional thermal model that solves the heat transfer equation using the finite difference method, which we combine with a spectral solution that accounts for the effects of topography on the shape of the isotherms[33]. The initial condition is a linear unperturbed geotherm. We then compute the depth of closure by extracting the cooling history of each sample and using Dodson's approximation[34]. Both the temperature field and Dodson's approximation depend on the solution (that is, estimated erosion rates), which implies that the problem is weakly nonlinear. We obtain the solution by direct iteration on the procedure we discuss below. Convergence occurs typically after a few iterations.

To obtain a useful numerical solution for equation (1), we discretize the integral. It becomes a summation in which erosion rate is parameterized as a piecewise constant function over fixed time intervals. A thermochronometric age is thus represented by a linear equation, and a suite of n thermochronometric ages becomes a linear system of independent equations:

$$A\dot{e} = z_c \quad (2)$$

where z_c becomes a vector of length n describing the different closure depths, $\dot{e}$ is a vector of unknown erosion rates and A is a sparse matrix whose components have units of time. This leads to an under-determined inverse problem, which can be solved by regularization (see ref. 35, for example). To that end, we impose the condition that erosion rates are correlated in space by defining an a priori covariance matrix, C. This covariance matrix is constructed for all time intervals using the horizontal distance d between the ith and jth data points, and an exponential correlation function:

$$C_{ij} = \sigma_e^2 e^{-\frac{d}{\lambda}} \quad (3)$$

where λ is a specified correlation length that we fix equal to 30 km. The a priori variance for the erosion rate, σ_e^2, serves primarily as a weighting factor. It is worth noting that this covariance matrix simply implies that samples close to each other must follow the same erosion history and that samples far apart may follow independent erosion histories.

In turn, it can be shown that the solution to our inverse problem for the erosion rate $\dot{e}$ is given by:

$$\dot{e} = \dot{e}_{pr} + CA^T(ACA^T + C_\varepsilon)^{-1}(z_c - A\dot{e}_{pr}) \quad (4)$$

where $\dot{e}_{pr}$ is the a priori expected value of the erosion rate and C_ε is a diagonal matrix containing the estimated data uncertainty. This corresponds to the common least-squares methods (see page 66 of ref. 36). We note that if the distance between each sample becomes infinitely small, the solution corresponds to a piecewise linear regression over each time interval, as illustrated in great detail in ref. 8.

This formal approach also has the advantage that it enables us to establish resolution by calculating the parameter resolution matrix, R:

$$R = CA^T(ACA^T + C_\varepsilon)^{-1}A \quad (5)$$

It provides us with a means of evaluating the correction to the prior model we obtain[35]. R is derived from the covariance we impose, the temporal discretization and the error in the data. The further away resolution is from identity, the worse the solution is. In this case, we are able to observe only a filtered version of the exact solution (pages 72–73 of ref. 36). For ease of visualization, we integrate R across the spatial dimension[8]. Results at data locations are then interpolated on a regular grid for visualization and to reduce weight due to the sampling density. The influence of various factors such as erosion rates are illustrated below.

Data compilation. We compiled thermochronometric data from across the globe for four systems: apatite (U–Th)/He (AHe), apatite fission track (AFT), zircon (U–Th)/He (ZHe) and zircon fission track (ZFT), which have closure temperatures of approximately 70 °C, 110 °C, 180 °C and 250 °C, respectively[19,37–40]. The data were extracted from the literature, and complemented with unpublished fission-track ages, together making a total of 17,833 ages. A full reference list is provided in Supplementary Information and all thermochronometric data are shown in Extended Data Fig. 1. We note that most fission-track ages were determined using the recommended external-detector method[41]. If they were not reported in the original publication, elevations were interpolated from a digital elevation model using the SRTM data[42] or Google Earth. We did not include track length measurements for the fission-track studies. This implies that we are likely to miss very recent changes in erosion rates, particularly in slowly eroding regions, that would be identified by a small population of long lengths. Further, track-length distributions are less discriminative in rapidly eroding terrains, because of associated generally young AFT ages. Furthermore, we are not trying to fit a single age but rather exploit the information contained in a sequence of ages from different thermochronometric systems and distributed with elevation[8].

Likewise, we did not include grain size for AHe and ZHe in our compilation. Grain size has an effect on He diffusion, because the size of the diffusion domain scales with grain dimensions (see refs 19 and 37 for example). Most grains analysed are typically about 60 μm (sphere-equivalent radius), or larger, to limit alpha-ejection correction[43]. Large grains (100–200 μm), may imply a closure temperature 5° to 8° higher than for 60-μm grains[37], which would lead to older measured cooling ages. Our inversion assumes a grain size of 60 μm, so we may underestimate the travel distance between closure depth and the surface. This does not affect our main conclusions because, in the worst-case scenario, the inferred increase would merely be undervalued.

The compiled data carry a degree of uncertainty that varies between publications. Methods used to estimate this uncertainty are rarely described. To avoid problems raised by the different methods and the associated level of analytical precision, we prescribed uniform uncertainties that are uncorrelated with ages in the inversion (note that using the analytical uncertainties does not modify our conclusions). More importantly, the inversion method we use enables us to treat data of mixed quality and uneven spatial distribution and establish resolution. In turn, it directly propagates the variance in the data into the model variance[8,35,36,44].

Sensitivity to prior erosion rates and initial geotherm. The erosion rate history we obtain using the linear inversion approach may depend on the choice of prior erosion rates (equation (4)). Although we may locally have some independent knowledge of erosion rates, in most cases we do not have any prior information other than from thermochronometric data. Therefore, we performed several inversions using different prior erosion rates. The results are shown in Extended Data Fig. 2a. They show that our inferred increase in erosion rates is weakly dependent on the prior erosion rates, further supporting the robustness of our results. It is also worth pointing out that choosing a prior erosion rate that is substantially different from the actual solution will lead to a wrong solution (not illustrated).

The linear inversion method includes a solution of the transient heat transfer equation (Methods[8]), which defines the depth of closure isotherms. As a result, the choice of thermal parameters may have an impact on the erosion rate history[8,19,45–47], particularly during the latest stage of exhumation. Therefore, we tested several inversions using different initial near-surface geothermal gradients. The results are shown in Extended Data Fig. 2b, which shows that one needs unrealistically high geothermal gradients (over 80 °C km^{-1}) everywhere to erase the increase in erosion rates we observe.

Limitations of using thermochronometry to derive changes in erosion rates. Thermochronology has several limitations for estimating erosion rates and how they vary with time. First, erosion rates inferred from a single thermochronometric age depend on the assumed geotherm, which defines the depth of the closure isotherm. In most cases, the geotherm is poorly known and a thermal model must be used, which may have an influence on the derived erosion rate, as discussed above. This can be circumvented, to some extent, by collecting samples at different elevations. In this case, the slope of the age–elevation relationship gives an estimate of the erosion rate at the timescale fixed by the measured ages[8,19,45–49], at least when heating advection, and therefore erosion rate, is not too large[50,51]. As explained in detail in ref. 8, the inversion scheme we adopt takes advantage of this, accounting for the effects of heat advection. Furthermore, we show above that one needs an anomalously high near-surface geothermal gradient to erase the global increase in erosion rates.

Second, a thermochronometric age only provides an estimate of the erosion rate integrated over the time defined by its apparent age[8,19,45–47]. Given that our objective is to detect changes in erosion rates through time, it is crucial to combine systems of different closure temperatures, in addition to age–elevation profiles. Unfortunately, disparate data sets have been collected for each system. To assess potential problems rising from the compiled data, including paucity of some data sets, we predict ages by running simulations using a one-dimensional thermal model[50] with a prescribed erosion history that varies over 2-Myr time intervals. We then couple this thermal model with a nonlinear inversion algorithm, namely the Neighbourhood algorithm[52,53] (see ref. 54 for details), to investigate whether we can recover the erosion histories using different thermochronometric systems. For completeness, we also use the linear inversion that we utilize for the global inversion. The results are presented in Extended Data Fig. 3.

The tests consist of four different simple erosion histories. In the first two (Extended Data Fig. 3a and b), we impose a background erosion rate of 0.1 mm yr^{-1} between 20 Myr ago and 2 Myr ago, followed by an increase in erosion rate to 0.9 mm yr^{-1} (Extended Data Fig. 3a) and 1.8 mm yr^{-1} (Extended Data Fig. 3b) over the past 2 Myr. For the two other tests (Extended Data Fig. 3c and d), we use a background erosion rate of 0.9 mm yr^{-1} between 20 Myr ago and 2 Myr ago that increases to 1.3 mm yr^{-1} (Extended Data Fig. 3c) and 1.8 mm yr^{-1} (Extended Data Fig. 3d). The vertical extent of the one-dimensional model is 30 km, with a bottom temperature of 900 °C, a thermal diffusivity of 30 km^2 Myr^{-1}, no radiogenic heat production and an unperturbed linear geotherm as the initial conditions. For each erosion history, we run three subsequent inversions: (1) an optimal case in which we have access to the four thermochronometric systems (AHe, AFT, ZHe and ZFT data), (2) a second case with access only to AFT and AHe data, and (3) a last scenario with AFT data only (which represents the largest amount of data currently available, Extended Data Fig. 1). The results are presented in Extended Data Fig. 3. Both approaches lead to similar erosion rate histories, keeping in mind that the solution of the linear inversion depends on the choice of prior erosion rates[8].

The inversion results show that erosion rates may be underestimated towards the present and overestimated back in the past when the background rates are low (0.1 mm yr^{-1}) and the change in erosion rate is not large (Extended Data Fig. 3a and b). Furthermore, a robust increase is more likely to be found at locations where data from several thermochronometric systems are available. These results imply that we may observe a smoother erosion history when erosion rates are too low, the increase is too small or where we do not have access to several thermochronometric systems. Therefore, regions where we observe a robust increase during the Late Cenozoic correspond mainly to areas where AFT, AHe or more data exist. Importantly, the results also demonstrate that we are more likely to miss an increase in erosion than to infer that one does not exist; the latter has been suggested to be a problem when using sediment accumulation curves as a proxy for erosion[3,4].

In regions where background erosion rates are high (around 1 mm yr^{-1} and higher), we obtain good constraints on erosion rates in the past 2 Myr, but we may have poor constraints on erosion rates in the past if we do not have access to higher-temperature systems (Extended Data Fig. 3c and d). This implies that it may be difficult to constrain erosion rates further back in time in tectonically active areas with sustained very high rates of erosion.

Resolution sensitivity to exhumation rates. Here we illustrate how resolution (Methods and ref. 8) may be used to determine under which conditions one is likely to be able to detect an increase of erosion. We focus on some samples from Patagonia[15]. This region was chosen because it exhibits a large south-to-north gradient in ages, which led the authors of ref. 15 to infer an increase of erosion in response to glaciation in northern Patagonia only. The suite of available AHe, AFT and ZFT data is shown in Extended Data Fig. 1 and 4. We performed two inversions, using the same parameters as for the global inversion. The first inversion includes all the available data and the second includes ZFT ages only.

The first inversion reveals higher erosion rates in northern Patagonia that increase towards the present (upper panels in Extended Data Fig. 5), which corroborates the interpretation of ref. 15. Furthermore, the associated resolution increases towards the present (lower panels in Extended Data Fig. 5). This is important because it implies that resolution degrades backwards in time, as already illustrated for the Dabie Shan example[8]. As a result, we are more likely to resolve changes in erosion rates towards the present than in the past. This is partly why we concentrated only on the recent erosion history (the past 8 Myr), although our global data set spans ages from a few hundred thousand years to several hundred million years.

In addition, we observe low erosion rates in southern Patagonia. In this part of the range, no changes in erosion rates can be resolved, as quantified by the resolution. This is simply because the ages are too old. These results are further illustrated with the second inversion (Extended Data Fig. 6), which includes only ZFT ages. In this case, most of the ages are too old to reveal a robust change in erosion rates. We note that it does not necessarily mean that there was no change in erosion rates. Instead, it may be that the changes were not large enough to be resolved. This is a similar situation to the high-northern-latitude regions, such as western Scandinavia, Baffin Island or Greenland, even though it is clear that glaciation significantly affected these landscapes, as we discuss in the main text. This problem is inherent to thermochronometry and cannot be changed. The advent of recent techniques that give us access to lower temperatures, such as $^4He/^3He$ (ref. 55) or luminescence thermochronometry[56,57], may help us to resolve this issue in the future.

Method sensitivity to changes in exhumation trajectory. Here we assess the potential impact of changes in exhumation trajectory. We present three examples of simulations with exhumation on a thrust fault with a dip angle of 30° and a 25-km-deep flat décollement. The velocity field is defined according to the fault-bend folding method[58]. We first run a three-dimensional thermokinematic model[54] to predict AHe, AFT, ZHe and ZFT ages. The models are run for 20 Myr. The vertical extent of the model is 30 km, the horizontal extent is 120 km long and 60 km wide and includes some topography that remains steady (Extended Data Fig. 7). We use a bottom temperature of 750 °C, a thermal diffusivity of 30 km^2 Myr^{-1}, no radiogenic heat production and an unperturbed linear geotherm as the initial condition. Pre-collisional ages are set to 100 Myr ago. We then select 70 ages randomly and run the linear inversion that we use for the global inversion. The first and second examples have slip rates of 5 mm yr^{-1} and 1 mm yr^{-1}, respectively. The third one has a constant slip rate of 1 mm yr^{-1} that increases to 5 mm yr^{-1} in the past 2 Myr.

The results are shown in Extended Data Fig. 8. First, they illustrate that one cannot constrain erosion rates where the ages are not reset (in general, that is over 20 Myr ago). The scenario with an erosion rate of 5 mm yr^{-1} is an example in which we infer the correct rates between 2 Myr ago and 0 Myr ago but underestimate rates between 6 Myr ago and 4 Myr ago (Extended Data Fig. 8a), as discussed above with the one-dimensional model. However, the resolution is low. In such a situation, the inferred increase would be excluded for our global interpretation. In contrast, if rates have remained relatively low or have increased since 2 Myr ago (Extended Data Fig. 8b and c), the resolution is high enough from 6 Myr ago to 0 Myr ago for us to detect an increase of erosion rates, which is again entirely consistent with the one-dimensional examples shown above.

33. Mancktelow, N. S. & Grasemann, B. Time-dependent effects of heat advection and topography on cooling histories during erosion. *Earth Planet. Sci. Lett.* **270,** 167–195 (1997).
34. Dodson, M. H. Closure temperatures in cooling geochronological and petrological systems. *Contrib. Mineral. Petrol.* **40,** 259–274 (1973).
35. Aster, R., Borchers, B. & Thurber, C. *Parameter Estimation and Inverse Problems* 2nd edn (Elsevier, 2012).
36. Tarantola, A. *Inverse Problem Theory* (SIAM, 2005).
37. Farley, K. A. Helium diffusion from apatite: general behavior as illustrated by Durango fluorapatite. *J. Geophys. Res.* **105,** 2903–2914 (2000).
38. Gleadow, A. J. W. & Duddy, I. R. A natural long-term track annealing experiment for apatite. *Nucl. Tracks Radiat. Meas.* **5,** 169–174 (1981).
39. Green, P. F. *et al.* Thermal annealing of fission tracks in apatite IV: quantitative modelling techniques and extension to geological timescales. *Chem. Geol.* **79,** 155–182 (1989).
40. Hurford, A. J. Uplift and cooling pathways derived from fission track analysis and mica dating: a review. *Geol. Rundsch.* **80,** 349–368 (1991).
41. Hurford, A. J. & Green, P. F. A users' guide to fission track dating calibration. *Earth Planet. Sci. Lett.* **59,** 343–354 (1982).
42. Farr, T. G. *et al.* The Shuttle Radar Topography Mission. *Rev. Geophys.* **45,** RG2004 (2007).
43. Farley, K. A., Wolf, R. & Silver, L. The effect of long alpha-stopping distances on (U-Th)/He dates. *Geochim. Cosmochim. Acta* **60,** 4223–4229 (1996).
44. Menke, W. *Geophysical Data Analysis: Discrete Inverse Theory* MATLAB edn, 3rd edn (Elsevier, 2012).
45. Ehlers, T. A. & Farley, K. A. Apatite (U-Th)/He thermochronometry: methods and applications to problems in tectonic and surface processes. *Earth Planet. Sci. Lett.* **206,** 1–14 (2003).
46. Ehlers, T. A. Crustal thermal processes and thermochronometer interpretation. *Rev. Mineral. Geochem.* **58,** 315–350 (2005).
47. Braun, J., van der Beek, P. A. & Batt, G. *Quantitative Thermochronology: Numerical Methods for the Interpretation of Thermochronological Data* (Cambridge Univ. Press, 2006).
48. Wagner, G. A. & Reimer, G. M. Fission track tectonics: the tectonic interpretation of fission track apatite ages. *Earth Planet. Sci. Lett.* **14,** 263–268 (1972).
49. Gallagher, K., Stephenson, J., Brown, R., Holmes, C. & Fitzgerald, P. Low temperature thermochronology and modeling strategies for multiple samples. 1: Vertical profiles. *Earth Planet. Sci. Lett.* **237,** 193–208 (2005).
50. Mancktelow, N. & Grasemann, B. Time-dependent effects of heat advection and topography on cooling histories during erosion. *Tectonophysics* **270,** 167–195 (1997).
51. Braun, J. *et al.* Quantifying rates of landscape evolution and tectonic processes by thermochronology and numerical modeling of crustal heat transport using PECUBE. *Tectonophysics* **524–525,** 1–28 (2012).
52. Sambridge, M. Geophysical inversion with a neighbourhood algorithm—I. Searching a parameter space. *Geophys. J. Int.* **138,** 479–494 (1999).
53. Sambridge, M. Geophysical inversion with a neighbourhood algorithm—II. Appraising the ensemble. *Geophys. J. Int.* **138,** 727–746 (1999).
54. Herman, F. *et al.* Exhumation, crustal deformation, and thermal structure of the Nepal Himalaya derived from the inversion of thermochronological and thermobarometric data and modeling of the topography. *J. Geophys. Res.* **115,** B06407 (2010).
55. Shuster, D. L., Farley, K. A., Sisteron, J. M. & Burnett, D. S. Quantifying the diffusion kinetics and spatial distributions of radiogenic ^4He in minerals containing proton-induced ^3He. *Earth Planet. Sci. Lett.* **217,** 19–32 (2004).
56. Guralnik, B. *et al.* Effective closure temperature in leaky or saturating thermochronometers. *Earth Planet. Sci. Lett.* **384,** 209–218 (2013).
57. Li, B. & Li, S.-H. Determining the cooling age using luminescence-thermochronology. *Tectonophysics* **580,** 242–248 (2012).
58. Suppe, J. Geometry and kinematics of fault-bend folding. *Am. J. Sci.* **283,** 684–721 (1983).

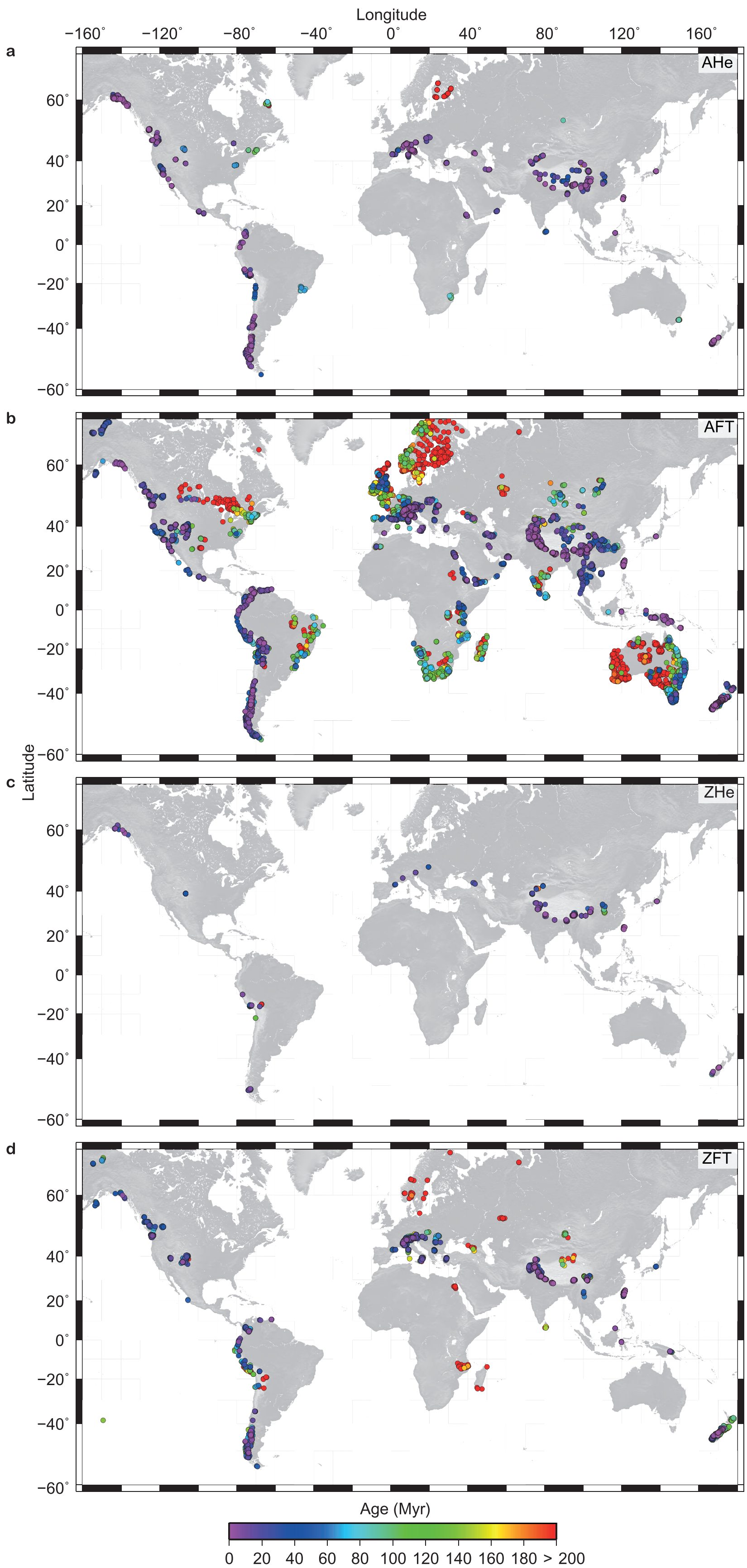

Extended Data Figure 1 | Compilation of thermochronometric ages. See the source data and associated references in the Supplementary Information for sample locations, elevations, ages and standard error measurements.

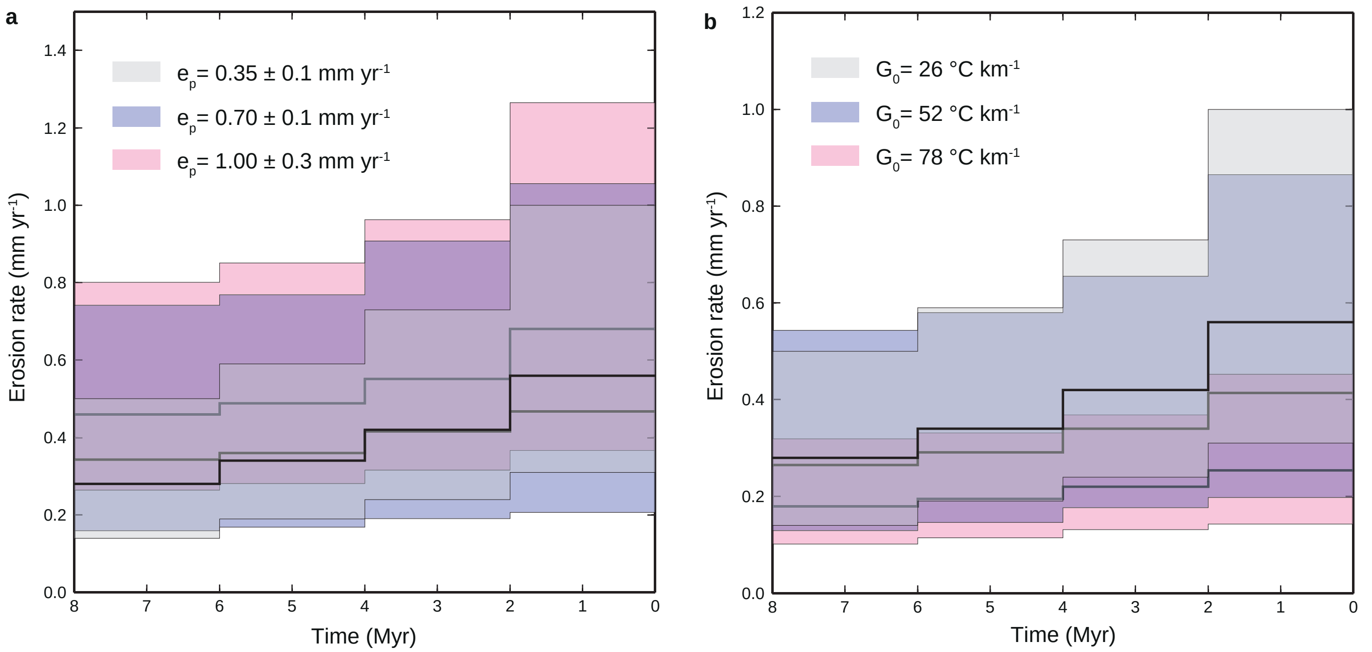

Extended Data Figure 2 | Global inversion sensitivity tests. a, Same as Fig. 3b, but using different prior erosion rates e_P (equation (4) in Methods), as indicated on the figure. **b**, Same as Fig. 3b, but using different initial near-surface unperturbed geothermal gradients G_0. See text for details.

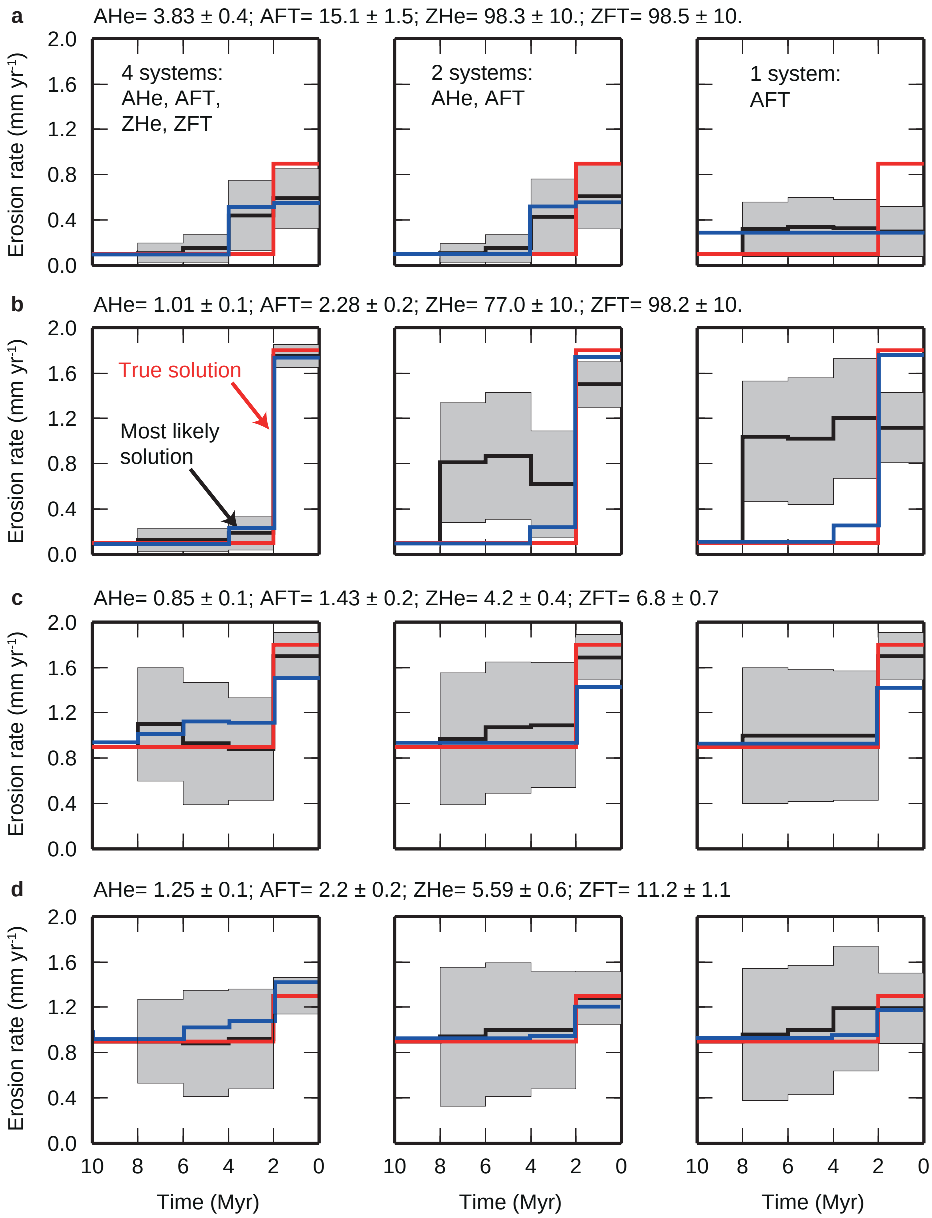

Extended Data Figure 3 | One-dimensional inversion results for four different erosion histories. The red curve is the erosion history used to generate synthetic thermochronometric ages. The ages (Myr) for each test are indicated on the figure. The black lines are the most likely solution obtained from the Bayesian inversion. The grey areas represent the 1σ uncertainty around the most likely erosion rate solution. The blue lines are the results of the linear inversion (Methods and ref. 8). The panels on the left depict inversion results using all four systems; the middle panels use AHe and AFT only; and the right panels use AFT only. See text for details.

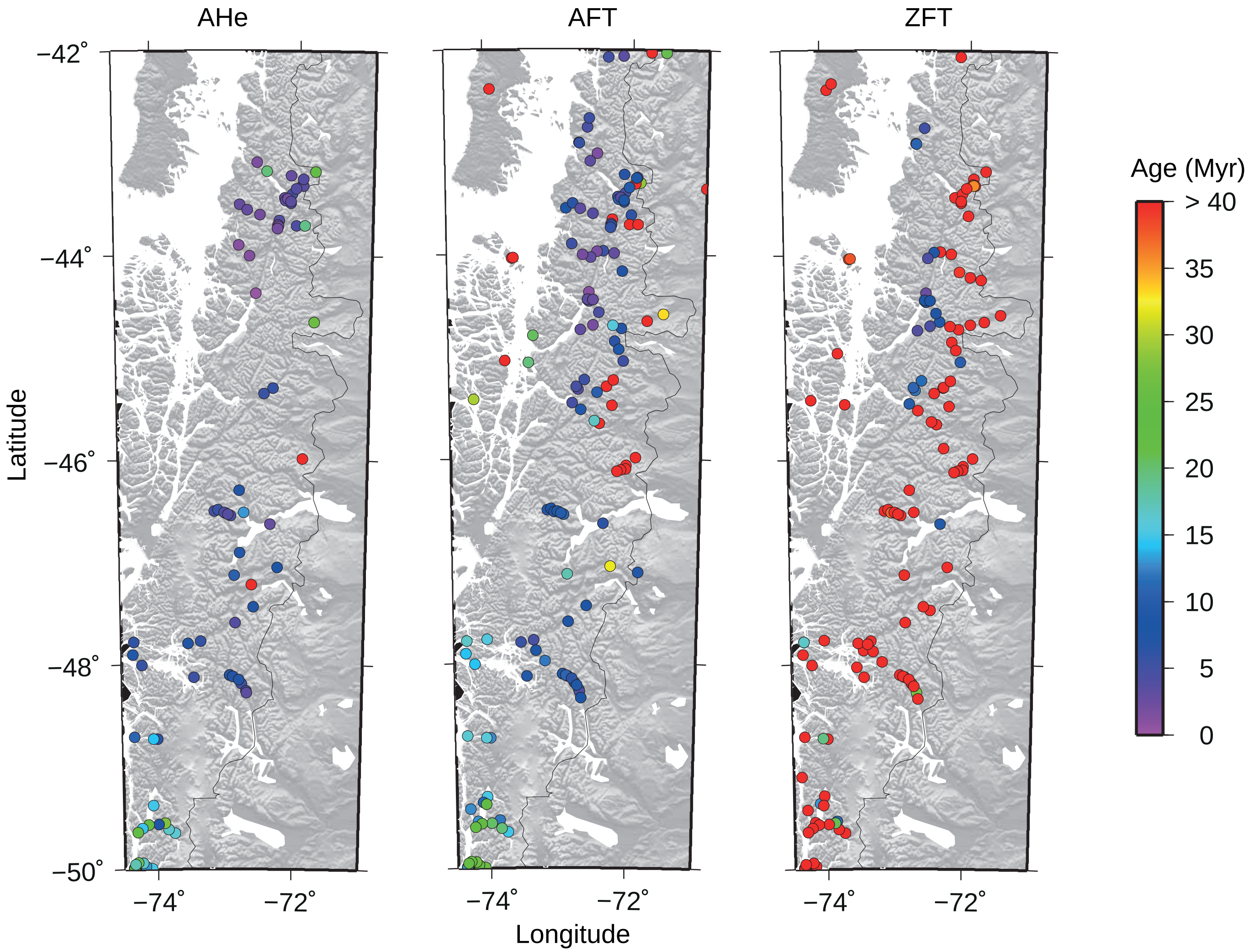

Extended Data Figure 4 | Thermochronometric data from Patagonia[15]. See Extended Data Fig. 1 and ref. 15 for further details.

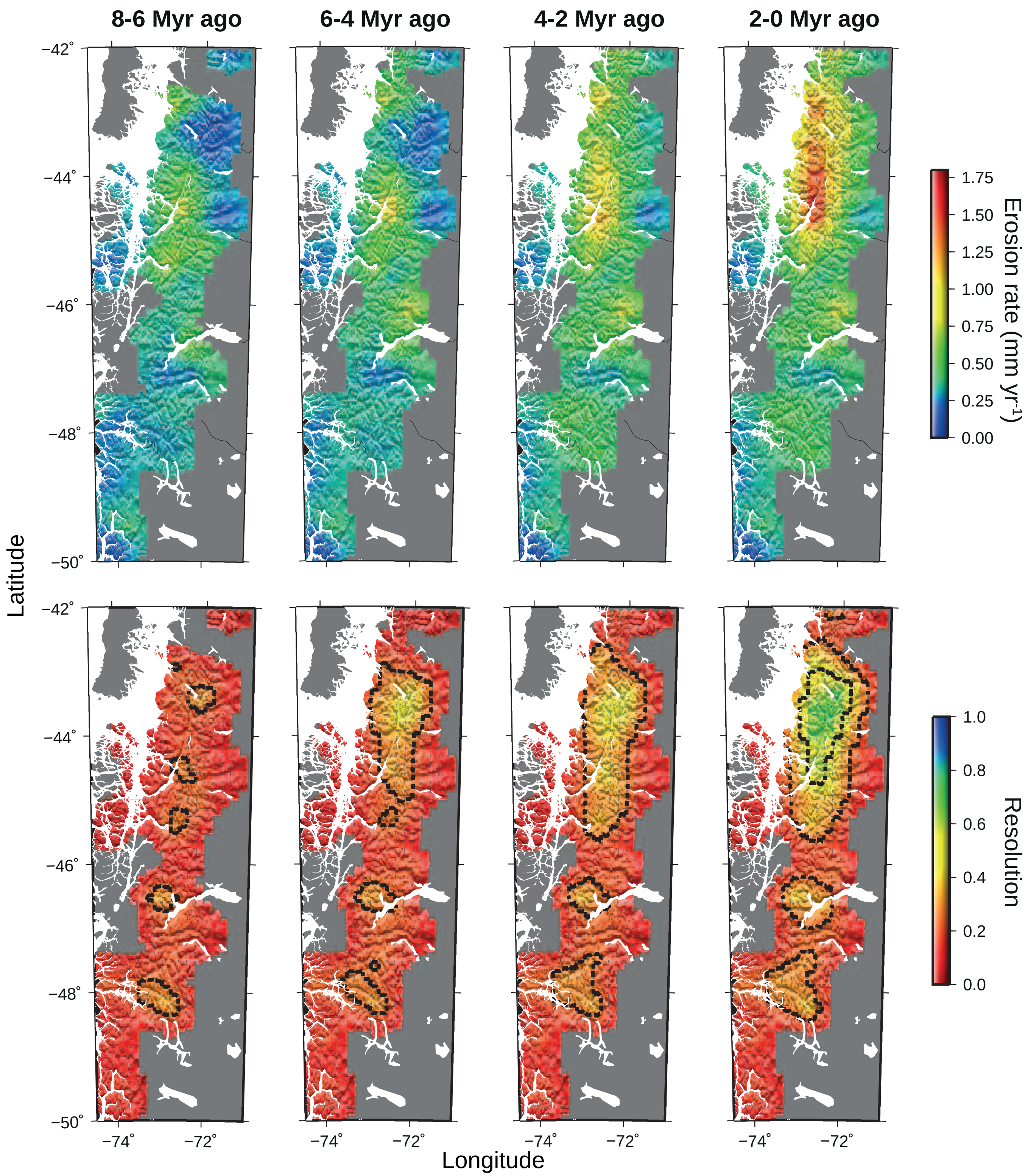

Extended Data Figure 5 | Inversion results of Patagonia thermochronometric data set[15]. The upper panels are erosion rates predicted by the inverse method[8]. The lower panels are resolution estimates (with 0.25 contours).

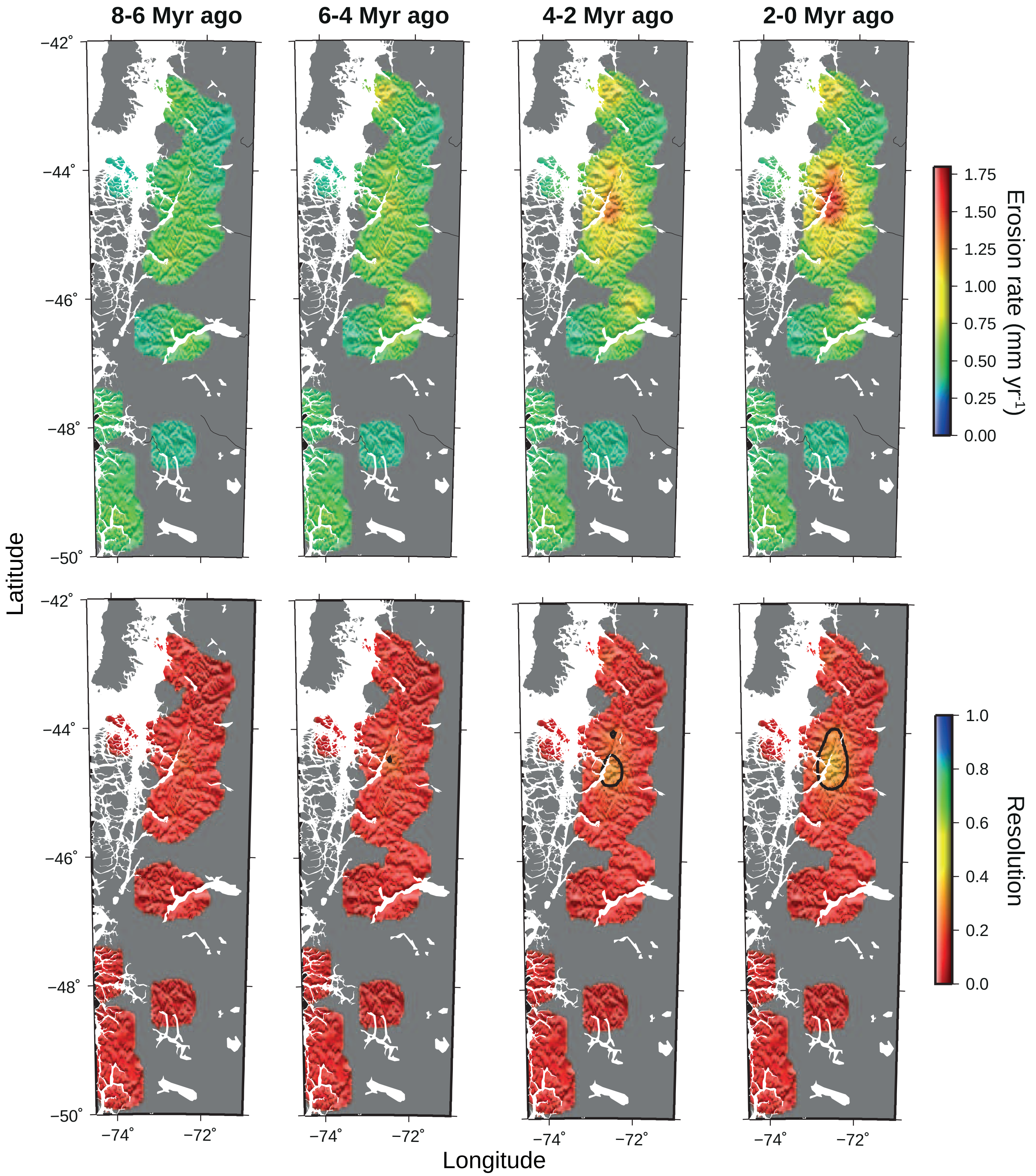

Extended Data Figure 6 | Inversion results of ZFT Patagonia data only. Upper panels are predicted erosion rates with the inverse method[8]. Lower panels are resolution estimates (with 0.25 contours).

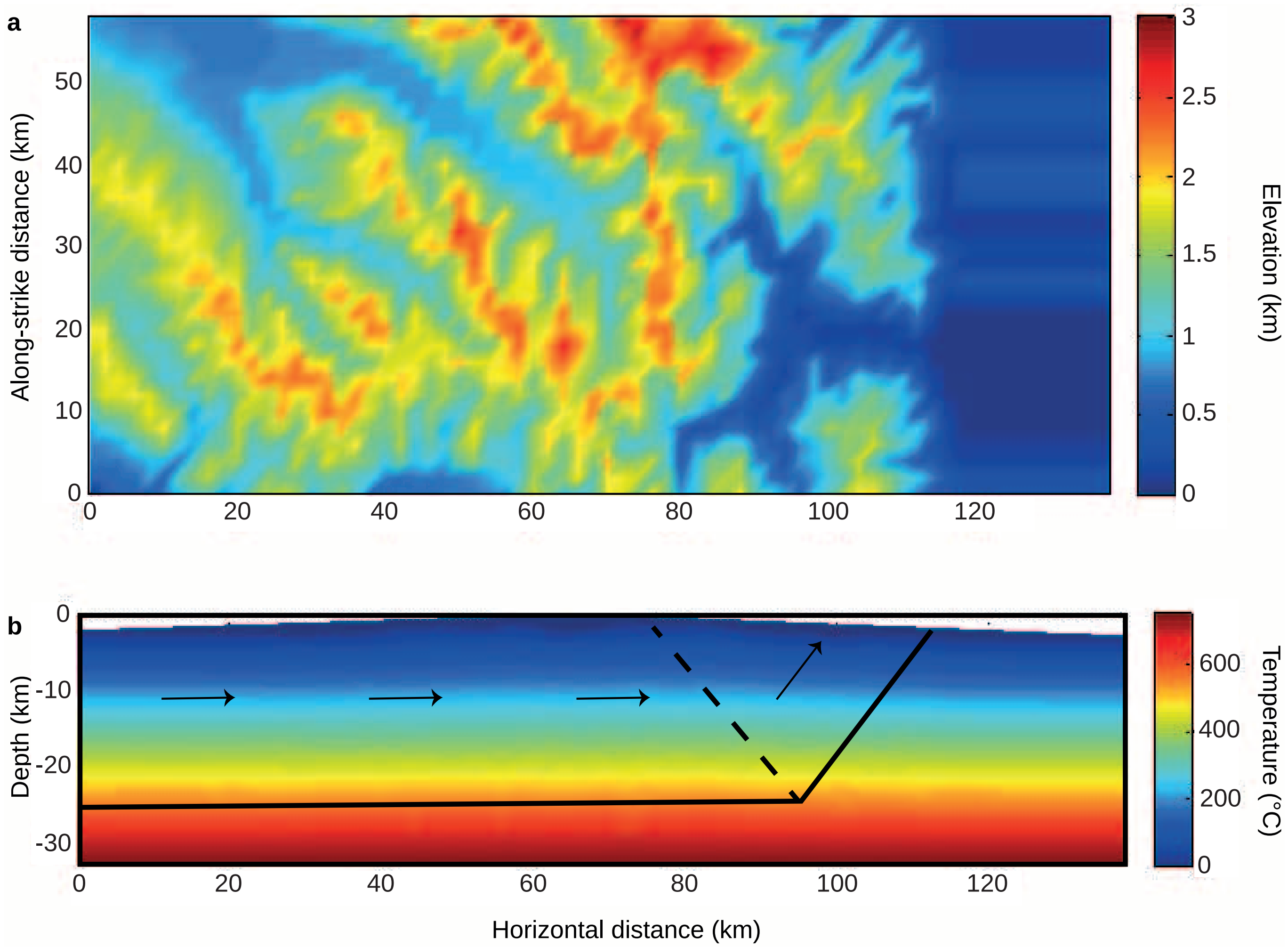

Extended Data Figure 7 | Set-up for the three-dimensional thermo-kinematic model. **a**, Topography and horizontal extent. **b**, Vertical extent, initial unperturbed temperature field and imposed kinematic field.

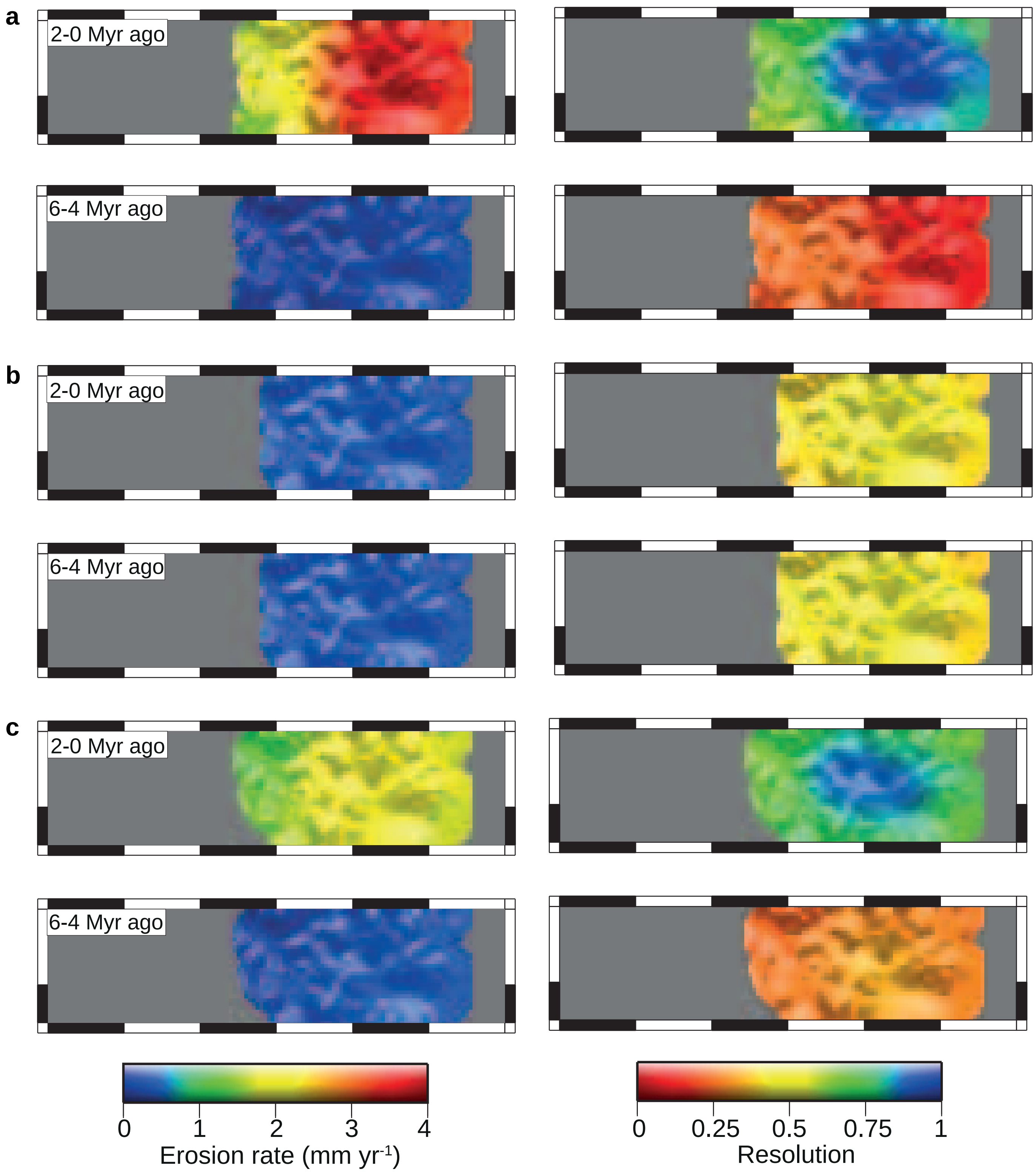

Extended Data Figure 8 | Inversion results on three-dimensional synthetic data. **a**, Inversion on synthetic data produced with constant 5 mm yr^{-1} slip rates. **b**, Same as **a** using a 1 mm yr^{-1} slip rate. **c**, Same as **b**, but with a slip rate that increases from 1 mm yr^{-1} to 5 mm yr^{-1} in the past 2 Myr. Left panels are erosion rates and right panels are resolution estimates.